Nonconcave grain micro-surfaces for reliable perovskite thin-film interfaces

Tong Xiao[1], Mingwei Hao[1], Tianwei Duan[1], Yanyan Li[3], Yalan Zhang[2], Peijun Guo[3], Yuanyuan Zhou[2*]

[1] Department of Physics, Hong Kong Baptist University, Kowloon, Hong Kong SAR, China

[2] Department of Chemical and Biological Engineering, The Hong Kong University of Science and Technology, Clear Water Bay, Hong Kong SAR, China

[3] Department of Chemical and Environmental Engineering, Yale University, New Haven, CT 06520 USA

*Correspondence should be addressed to: yyzhou@ust.hk

The surface of individual grains of metal halide perovskite films can determine the properties of heterointerfaces at the microscale and the performance of resultant solar cells. But the geometric characteristics of grain surfaces remain rarely investigated. Here we elaborate on the existence of grain surface concaves (GSCs) and their effects on charge-extracting, chemical, and thermomechanical properties of the buried perovskite heterointerfaces. The evolution of GSCs is triggered by grain-coalescence-induced biaxial tensile strain (BTS) and thermal-coarsening-induced grain-boundary (GB) grooving. As such, GSCs are tailorable via the regulation of grain growth kinetics. As a proof of concept, we used tridecafluorohexane-1-sulfonic acid potassium to alleviate BTS and GB grooving via molecular functionalization, forming non-concaved grain micro-surfaces. The resultant PSCs demonstrate enhanced power conversion efficiencies (PCE), together with elevated PCE retentions under ISOS-standardized thermal-cycling (300 cycles), damp-heat (660 h), and maximum-power-point tracking (1290 h) tests. This work sheds light on micro-surface engineering for improving the durability and performance of PSCs and optoelectronics.

Introduction

Perovskite solar cell (PSC) has recently been recognized as the most promising future photovoltaic technology in a wide range of application scenarios including building-integrated photovoltaics, as it combines the merits of potentially low manufacturing cost and high-power conversion efficiencies (PCEs). The certified record PCE of PSCs has been rapidly climbing in recent years, continuously injecting excitement into the photovoltaic industry.[1-3] Nevertheless, there is still an outstanding concern on the long-term durability of PSCs in practical operating conditions with complex stressors of light, heat, and moisture,[4-6] calling for an in-depth fundamental investigation on the microscopic structure-property-performance relationships.[7-9] Currently, there are numerous studies have suggested that device heterointerface plays a dominating role in the long-term durability of PSCs.[7,10,11] Attainment of ideal microstructural and functional integrity at device heterointerfaces is thus a key step to optimize the carrier injection and thermal management, to minimize the moisture ingression, and to mitigate the mechanical failure due to interfacial fatigue as well as accumulated thermal stress.

Interfacial engineering has so far become the most successful method to achieve PSCs with the best PCEs, chemical stability, and thermomechanical reliability.[12-14] The reported studies have a primary focus on chemical passivation on perovskite top and bottom (also referred as "buried") surfaces/interfaces, to lower the defect density, to manipulate energy level alignment, to enhance the phase purity, etc. However, insights into the microstructural integrity of these heterointerfaces are usually missing, which eventually dictates the functional properties.[7] Especially, the perovskite heterointerfaces have been generally treated as an ideally continuous and flat microstructure type. In fact, perovskite thin films in state-of-the-art PSCs are invariably polycrystalline, consisting of a dense packing of individual grains. As a result, the heterointerface of perovskite with the charge-transport layer (CTL) can be viewed as an ensemble of grain-CTL micro-heterointerface "segments". The properties of each grain-CTL micro-heterointerface accumulatively determine the properties of the overall heterointerface. Therefore, it is critical to ensure the high microstructural integrity of individual grain-CTL micro-heterointerfaces so that a more ideal perovskite heterointerface can be formed.

In this work, by using careful atomic-force microscopy and depth profiling, we revealed a general existence of grain surface concaves (GSCs), a type of under-explored microstructure, on individual grain surfaces of representative perovskite films. These GSCs inevitably lead to buried nanoscale gaps between the grain center and the underneath CTL. Due to their relatively small depths as compared to the sizes of individual grains and the height contrast of grain boundary grooves (GBGs), it is not surprising that GSCs have been neglected in the morphological and microstructural studies of PSCs in the past years. We found that the formation of these GSCs is attributed to the solid-state ion plastic flow from the GBGs and the grain surface center to the convex ridges, which are triggered by thermal-driven grain boundary (GB) grooving and grain-coalescence-induced biaxial tensile strain (BTS), respectively. More importantly, GSCs impart profound negative effects on carrier-exacting, chemical, and thermomechanical properties of perovskite heterointerface. Herein we note that owing to the layer-by-layer nature of PSC processing, any negative effects on the structural and functional integrities on the perovskite top surface side are possibly compensated by a conformal deposition of sequential layers. This study thus focuses on the buried bottom perovskite heterointerface. To alleviate the negative effects of GSCs, we chose an anionic surfactant molecule, tridecafluorohexane-1-sulfonic acid potassium (TFSAP), to manipulate the interfacial energetics on grain surfaces and GBs to simultaneously suppress GB grooving and BTS. As a result, we achieved perovskite thin films with minimum GSCs observed on individual grains bottom surfaces, leading to the robust and stable grain-CTL micro-heterointerfaces. PSCs incorporating this microstructural engineering deliver a high PCE of 25.5%. The PCEs of PSCs with the removal of GSCs can retain 83%, 90% and 90% in device stability tests following international consensus protocols of ISOS-T-3 (300 cycles), ISOS-D-3 (660 h), and ISOS-L-11 (1290 h), respectively, demonstrating the merits of GSC engineering.

Geometric characteristics and chemical tailoring of GSCs

Herein we deliberately prepared two formamidine-cesium (FA-Cs) perovskite film samples ($FA_{0.9}Cs_{0.1}PbI_3$ composition) with an ITO/SnO_2/perovskite structure. One (pristine film) is from an additive-free perovskite solution while the other (target film) is from a perovskite solution with the addition of TFSAP, an anionic surfactant. The unique molecular characteristics of TFSAP enable it to moderate the microstructural evolution and to yield perovskite grains with minimum GSCs on bottom surfaces, which will be elaborated later. After the film fabrication, we mechanically delaminated the perovskite layer from the SnO_2 electron transport layer (ETL) using a method schematically illustrated in **Supplementary Fig. 1**. We then employed high-resolution atomic force microscopy (AFM) to characterize the flipped perovskite film bottom surface for quantitatively investigating the geometric characteristics of grain surface microstructures originally at the perovskite-CTL heterointerface. **Figure 1a**-**b** exhibit AFM topographies of perovskite surfaces with and without GSCs, respectively. For the pristine perovskite film, a polycrystalline microstructure is observed with high-contrast GBGs formed between packed individual grains and with GSCs emerging on most grains. The GSC microstructure is distinguishable by the peripheric region higher than the central region in a specific grain in a regular film. In contrast, GSCs are rarely observable on the grain micro-surfaces of the target film. By showing a narrow slice of the AFM 2D/3D image (**Figure 1 c-f**) that goes across one typical entire grain and adjacent GBs, we compare their detailed and localized geometric characteristics. For the pristine film, the grain contains a concaved center surface surrounded by convex ridges and GBGs, while the grains deliver nearly flat micro-surfaces for the target film. **Figure 1 g-h** exhibit the quantitative results from the height/depth line-profiling in **Figure 1 c-d** and in SnO_2 surfaces in **Supplementary Fig. 2a**, which further attests to the minimization of GSCs as well as the flattening of GBGs once the TFSAP additive is used for the film processing.

Next, we elaborate on the structure of grain-CTL micro-heterointerface. We obtained AFM images of the SnO_2 top surface before and after delamination, as illustrated in **Supplementary Fig. 2**. Because it is not practical to obtain correlated AFM images of SnO_2 ETL tops and perovskite bottoms all exactly from the same location in the film structure, we acquired a series of AFM images within a pre-labelled small area of the film, finding that the spatial differences in morphologies may be considered negligible. SnO_2 ETL top surfaces exhibit extremely low surface height fluctuations as compared with grain bottom surfaces, allowing them to be approximately treated as flat when assessing micro-heterointerface. This implies that for the pristine film case, when perovskite grains bottom surfaces are in contact with the SnO_2 ETL top surfaces, the concaved grain center could inevitably result in nanoscale gaps, which are localized by the grain periphery. Such nanogaps exhibit relatively small depth dimensions, making them hardly observed in top-view and cross-sectional SEM images (**Supplementary Fig. 3-4**). In contrast, when GSCs are minimized in the target films, a high integrity in the grain-CTL micro-heterointerface is achieved. **Supplementary Fig. 5** illustrates even similar nanoscale morphologies of the perovskite grain bottom and SnO_2 top surface in the target film, indicating a strong structural coherence because of an intimate interfacial contact. We excluded the possibility of such morphology of the perovskite grain bottom being caused by TFSAP aggregates, as we applied an isopropanol solvent washing and observed no morphological change (**Supplementary Fig. 6**). Note that these GSCs-induced nanovoids should be considered different from the GBGs-induced and solvent-trapping-induced voids on buried heterointerfaces earlier reported in literatures.[15-19] As shown in **Figure 1e**, GSCs-induced nanogap can span almost the whole grain, and it has truly statistical significance as it exists on almost every regular grain. In contrast, GBGs-induced void is only horizontally across a few tens of nanometers.[17] The solvent-trapping-induced void is mostly a type of microscopic or macroscopic volume defect that randomly exists at the heterointerface.[15,20]

To assess the microstructural tailoring effect of TFSAP, as schematically illustrated in **Figure 1i**, we introduced a new geometric parameter ξ in addition to the GBG angle θ defined previously.[17] θ represents the angle between the tangent to the GBG side and the horizontal direction. ξ represents the angle between the line connecting the apex of the convex ridge to the center of the GSC and the horizontal direction, thus roughly elaborating the degree of the curving from an ideally flat surface. We totally conducted 60 and 80 measurements to obtain the ξ and θ statistics for each film, respectively (**Figure 1j-k**). The pristine film contains GSCs with an average ξ value of 2.09°. In contrast, the target film exhibits significantly reduced ξ, with most values distributing within the range of 0° to 1° (0.47° on average), in which context all the grains can be considered non-concaved. It is also interesting that the GBG angle θ shows the same trend as the GSC angle ξ with the TFSAP addition. The target film exhibits flattened GBGs with an average θ value of 9.9°, decreased from 15.9° for the pristine film. These results confirm the effectiveness of the TFSAP on the microstructural tailoring of perovskite grain surface. Although the changes of GSC and GBG angles (ξ and θ) are coupled due to their inherent formation mechanisms (to be elaborated later), we expect that the minimization of GSCs can become a crucial factor in addition of GBG flattening [17] in constructing perovskite heterointerfaces with ideal microstructural and functional integrities, especially considering their original lateral dimensions.

Analysis of the formation and evolution of GSCs

We propose that the evolution of these GSCs is attributed to two main mechanistic factors, as schematically illustrated in **Figure 2a**. The first factor is the intrinsic BTS generated by the grain coalescence during the solution crystallization stage (left panel). The other is thermal-driven GB grooving during the grain coarsening stage (middle panel). Triggered by both processes, solid-state ion plastic flow can occur from the grain surface center and GBG regions to the convex ridges, contributing to the evolution of GCSs (right panel). Below we elaborate on the detailed mechanisms.

Once a perovskite grain is formed from the solution, it is expected to grow until getting in contact with adjacent grains, leading to the generation of the interatomic forces,[21] and accordingly BTS:

$$\varepsilon_{xy\_BTS} = \left[4a\left(2\gamma_s - \gamma_{gb}\right)\frac{1-\upsilon}{M} \right]^{\frac{1}{2}} \tag{1}$$

$$\varepsilon_{z\_BTS} = \upsilon \cdot \varepsilon_{xy\_BTS} \tag{2}$$

where a is the half of the grain size, γ_s is surface free energy per unit area, γ_{gb} is GB energy per unit area, M is the Young's modulus, and v is the Poisson's ratio. This BTS will lead to the ion flow from the grain center towards the sides, accordingly generating the out-of-plane deformation (ε_{z_BTS}). Based on these, the theoretically estimated ε_{z_BTS} is at the nanometer scale, which is consistent with experimentally measured deformation (ε_z) from the AFM depth profiling (**Figure 1g**). The relative difference between ε_{z_BTS} and ε_z can be partly attributed to the contribution of the thermal-driven GB grooving which has not included yet. Once grains have coalesced, GB grooving begin to dominate GSCs formation, while the contribution to the out-of-plane deformation by GB grooving ($\varepsilon_{z\_grooving}$) is still hard to quantify at this time. Notably, GSCs more profoundly exist on perovskite bottom surface than top surface, as the top surface is freely grown without a geometric boundary condition as we set for the bottom surface (**Supplementary Fig. 7**).

To attest the above elaborated theory coincides with our experimental observations on GSC formation, we have also excluded the possibilities of other potential factors dominating the GSCs formation. First, we explored the effect of substrate roughness. **Supplementary Fig. 8** shows the representative AFM images of perovskite thin films fabricated on FTO and silicon wafer substrates which present much higher and lower roughness than SnO_2 ETL, respectively. GSCs are generally observed in both cases, despite a difference in the detailed geometries. Then, although there are occasional bulges on the SnO_2 ETL surface, they cannot be a major contributing factor, either, considering the substantial difference in the geometric characteristics between the bulges and GSCs (**Supplementary Fig. 9**). Third, since the perovskite bottom surfaces for AFM characterization are obtained from a mechanical peeling process, nanofragments from perovskite surface may be peeled off, which can influence the bottom surface geometry. But such nanofragments of no statistical significance are experimentally found to be mostly taken from the GBG region of the perovskite bottom surface (**Supplementary Fig. 10)**.

Based on the consolidated theory, as known from Equation (1), to minimize GSCs, we will need to reduce the out-of-plane deformation ε_{z_BTS} by minimizing $(2\gamma_s - \gamma_{gb})^{1/2}$. This rationalizes our employment of the surfactant molecule TFSAP additive to tailor the GB and surface energies.[22,23] As shown in **Figure 2b** left panel, in TFSAP, the organic anion possesses two functional groups, a short all-fluorinated carbon chain and a sulfo group. Regarding the K^+ cation, it does not impose a notable effect on microstructure and surface morphology, as supported by the AFM observations when an alternative additive of KI applied at the same concentration (**Supplementary Fig. 11)**. The organic anion of TFSAP tends to homogenously interact with the perovskite grains surfaces and GBs via the head-tail configuration (**Figure 2b** middle panel), which can be attributed to two factors: (i) the polar, electron-rich sulfo group can anchor on the iodide vacancies; (ii) the all-fluorinated carbon chain contains maximum electron pairs that could effectively prevent self-aggregation. Therefore, TFSAP can reduce the surface and GB energies, as well as the difference between the two. We experimentally determined γ_s using the standard OWRK method [24] and then γ_{gb} based on the width-depth (*w*-*d*) relationship of the Mullins' GBG model.[25] The contact angle images with water and diiodomethane are collected in **Supplementary Fig. 12**. The values of contact angle are listed in **Supplementary Table 1.** The associated method details are illustrated in the **Methods**. The obtained γ_s, γ_{gb} and $\Delta\gamma$ ($2\gamma_s$ - γ_{gb}) are shown in **Figure 2c**, and the normalized ε_{z_BTS} are shown in **Figure 2d.** As expected, there are decreases of γ_s from 0.047 to 0.029 N m^{-1}, and γ_{gb} from 0.031 to 0.015 N m^{-1}, leading to the decrease of normalized ε_{z_BTS} from 1.00 to 0.82. TFSAP, with sulfonic acid groups rich in electron pairs, can form coordination bonds with Pb atoms to segregate on the grain surface and GBs. Simultaneously, this chemical interaction can also inhibit the surface diffusion of solid-state ions. Since the solid-state ion flow is mainly mediated by surface/interface vacancies, as illustrated in **Supplementary Fig. 13**, by passivating these vacancies, the ion flow may be inhibited. The inhibition effect on ion flow could be also related to the size of the molecules, as a larger molecule can serve as a kinetically more stable barrier for the solid-state ion flow. Therefore, the solid-state ion flow in the GB grooving process can be greatly alleviated (**Figure 2b** right panel).[17] These results well support our proposed mechanism for GSC microstructural evolution and elucidate the role of TFSAP. In addition to using TFSAP, we also used two other surfactant molecules Pluronic® P-123 and N,N,N-Trimethyloctan-1-aminium chloride (NTAC), finding similar effects on the grain micro-surface (**Supplementary Fig. 14**). Specifically, the -OH groups at the two tails of Pluronic® P123 can form relatively weak hydrogen bonds with organic FA^+ cations in perovskite, while the quaternary ammonium cations of NTAC can interact with iodide ions in perovskite. These interacting surface molecules tailor the interfacial energies to relax BTS and hinder ion flow, thus leading to the GSC elimination. Therefore, our proposed mechanism applies to the P123 and NTAC cases, regardless of their distinct molecular structures and different interaction modes with perovskite grains. These reflect that our GSC approach can be generic and there is space for future optimization.

GSC effects on heterointerfacial properties

Then we assessed the optoelectronic and chemical properties of the perovskite-CTL heterointerfaces before and after the GSC engineering. The steady-state photoluminescence (PL) spectra of both perovskite films on quartz substrates are shown in **Figure 3a**, which indicate significantly reduced nonradiative recombination in the presence of GSCs, attributing to the physical passivation effect on free surfaces in GSCs to reduce trap densities.[26,27] We further acquired time-resolved PL (TRPL) spectra in **Figure 3b** for both films with and without GSCs deposited on SnO_2-ETL-coated ITO. We found that the average PL lifetime (τ_{avg}) decreases from 32.7 to 14.8 ns in the absence of GSCs, suggesting the electron-extracting properties of the perovskite heterointerface are strongly enhanced. The steady-state PL measurements based on the ITO/SnO_2 ETL/perovskite sample structures also show consistent results (**Supplementary Fig. 15**). To quantitatively measure the trap density, we performed space-charge-limited current (SCLC) measurements on both perovskite films, as shown in **Figure 3c**. The value of trap-filled-voltage (V_{TFL}) decreases from 0.122 to 0.088 V, corresponding to a decrease of trap density from 1.499×10^{14} to 1.082×10^{14} cm^{-3} after the GSC engineering. We also conducted PL measurements on flipped, delaminated perovskite films, as shown in **Supplementary Fig. 16**. For the target film, the peak intensity of the steady-state PL spectrum is higher. The photocarrier lifetime (578 ns) fit from the TRPL spectrum is also longer than that for the pristine film (99 ns). Both suggests a lower intensity of trap states on the bottom surface of the target film. We further measured PL spectra from the bottom sides of both pristine and target films deposited on SnO_2 ETL coated quartz substrates. We observed a more effective PL quenching in the target film (**Supplementary Fig. 17**). **Figure 3d**-**e** show the comparison of the optical absorption spectra of both perovskite films with and without GSCs under accelerated aging tests (3-sun-intensity, and 80°C). According to the normalized absorbance variations at the wavelength of 700 nm for both films (**Supplementary Fig. 18**), the target film shows only a marginal decrease in absorbance and the film color remained black, while the pristine film degraded quickly. This is consistent with our hypothesis that the GSC-induced nanovoids can serve as initial degradation sites since a free bottom surface tends to suffer more severely from photothermal and environmental stresses, which aligns with that of inter-grain nanovoids in earlier studies.[15,17,28] PL mapping images and X-ray diffraction (XRD) patterns in **Supplementary Fig. 19-20** also attest to the enhanced chemical stability after the GSC engineering. There could be also a positive contribution of the TFSAP chemical functionalization on these properties, *e.g.* moisture tolerance (**Supplementary Fig. 21**), which can be considered in addition to the effects of transformed grain micro-surfaces.

Next, we investigated the crucial thermomechanical properties of the perovskite-CTL heterointerfaces. We performed infrared-pump visible-probe (IPVP) transient absorption (TA) spectroscopy [29] to assess the heat-transfer dynamics of heterointerfaces with and without GSCs, with associated details illustrated in **Methods**. The differential change in transmittance (dT/T) can assess the heat-transport ability. [29] **Figure 3f-g** show the variation of dT/T under different delay time. The heterointerface without GSCs exhibit an enhanced decrease as compare with pristine samples, corresponding to faster heterointerfacial heat-transfer. It reveals that GSC-induced nanovoids hinder heat-transfer in heterointerfaces. **Supplementary Fig. 22** illustrates the constructed micro-interfacial models for calculating thermal conductivity *k*, where nanogap is simplified as a rectangle air gap. The overall *k* increase from 0.287 with GSCs to 0.358 W m^{-1} K^{-1} in the absence of GSCs, supporting the results obtained in IPVP TA experiments. We further employed finite element analysis (FEA) based on the models in **Supplementary Fig. 23**, and the 2D temperature distribution is shown in **Figure 3h** and temperature-line profiles are shown in **Supplementary Fig. 24** with a case of internal thermal source. The strongly increased temperature and the inhomogeneous out-of-plane distribution are observed in the nanogap region, proving that GSCs not only act as an interfacial thermal resistance for vertical interfacial heat transfer but also induce non-uniform temperature distributions at the grain bottom. The temperature distribution as a case of an external thermal source delivers the same conclusion, as shown in **Supplementary Fig. 25**. As a result of these effects, heat accumulation is expected in the pristine perovskite film, potentially leading to thermochemical and thermomechanical issues during the device durability tests, under two kinds of thermal gradients of internal and external heat sources. In addition, **Supplementary Fig. 26** reveals the thermal stress accumulation at the junction point under the deformation of micro-heterointerface with GSCs at -40°C and 85°C, which is the other stressors to break the mechanically grain-CTL connection under severe temperatures in the thermal cycling test.

For assessing the mechanical reliability at the perovskite-CTL heterointerface,[30] we employed a tape test based on the ASTM D3359 standard. This international standard is widely used to assess the adhesion reliability of a film to a substrate. The experimental process is schematically illustrated in **Figure 3i**. Here, standard perovskite grids (1×1 mm^2) were manually prefabricated onto the film by blades. Then we use the glass substrate with epoxy at the corners as the tape to delaminate perovskite grids from the SnO_2 CTL surface. The normalized delaminated area can qualitatively reflect the mechanical adhesion strength of the perovskite grains onto the SnO_2-ETL-coated ITO. **Figure 3j-k** are photographs of residual perovskite grids (on SnO_2-ETL-coated ITO) for the pristine and target cases, which clearly reflect the stronger film adhesion in the absence of GSCs. The statistical distributions of normalized delaminated areas for both perovskite films are shown in **Figure 3k**. The GSC engineering decreases the mean values of normalized delaminated areas from 0.740 to 0.524. We attributed the enhancement in overall film mechanical reliability to the accumulation of individual micro-heterointerfaces where grains have been in full contact with the SnO_2 ETL. While herein the chemical interaction of TFSAP with perovskite and SnO_2 may contribute to the improved adhesion strength, it is not considered as a dominating factor. To support this, we employed P123 and NTAC as the processing additive which led to a similar elimination of GSCs, but these additives are not expected to exhibit very profound chemical interaction with either SnO_2 or perovskite. Nevertheless, a similar level of improvement in interfacial adhesion strength to that caused by TFSAP is observed (**Supplementary Fig. 27)**. In the meanwhile, when we used potassium trifluoromethanesulfonate (PTFS) containing the same functional group as TFSAP while cannot flattening GSCs (**Supplementary Fig. 28**), we did not observe a notable improvement in the adhesion strength (**Supplementary Fig. 27**). The benefit of the non-concaved grains can be further amplified when an interfacial molecular glue is used, which in turn attests to the microstructural effects. We tested a reported interfacial glue of iodine-terminated self-assembled monolayer (I-SAM), (3-iodopropyl)trimethoxysilane ($Si(OCH_3)_3(CH_2)_3I$) [13] between perovskite grains and ETL. As shown in **Figure 3l**, with the I-SAM, the target film can demonstrate a further boosted interfacial adhesion, with the mean value decreasing from 0.291 to 0.118. It can be observed that I-SAM deposition on SnO_2 ETL surface can have a more profound contribution to the interfacial reliability enhancement, as compared to GSC minimization solely. Nevertheless, as GSC minimization increases the interfacial contact area, it further facilitates the formation of more effective interfacial hydrogen bonds via I-SAM incorporation. To provide a more intuitive illustration, we grouped the delamination experiment results according to the ASTM D3359 standard to rating the adhesion, ranging from scale 0B to scale 5B, where 0B represents the worst while 5B represents the best adhesion strength, as shown in **Figure 3m**. The distribution of 0B-5B matches the results **Figure 3l,** where target group without GSCs overall obtained a better adhesion scale. We expect that the flat grains create more molecular bonds in the grain centers, thus demonstrating interfacial adhesion, as shown in **Supplementary Fig. 29.** These results show that minimizing GSCs not only enhances the mechanical reliability on perovskite-CTL heterointerface but also imposes an additional positive effect on the established SAM-based interfacial engineering.

GSC effects on device performance and durability

We evaluated the effects of minimized GSCs on device photovoltaic and durability performances with the conventional device structure of ITO/SnO_2 ETL/Perovskite film/Spiro-OMeTAD/Au. **Figure 4a** shows the current density-voltage (*J*-*V*) curves of the champion PSC devices at reverse scan for both pristine and target films. To explore the efficiency potential, minimizing GSCs at grain-CTL heterointerfaces has significantly improved the optoelectronic performance of devices, leading to a PCE of 25.5% with an open-circuit voltage (V_{OC}) of 1.21V, a short-circuit current density (J_{SC}) of 25.69 mA cm^{-2}, and a fill factor (FF) of 0.82. The external quantum efficiency (EQE) spectrum of this PSC device with an integrated J_{SC} of 24.60 mA cm^{-2} is shown in **Figure 4b**, demonstrating a consistent integrated current density. For comparison, the champion PSC made with the pristine film shows a PCE of 23.3% with a V_{OC} of 1.17 V, a J_{SC} of 25.17 mA cm^{-2}, and a FF of 0.79. **Figure 4c** shows the PCEs statistical distributions of devices with and without GSCs. The significant improvement of V_{OC} and FF can be explained by the boosted electron-extraction and reduced non-radiative recombination in perovskite films without GSCs (**Figure 3a-c**). We attribute this improvement mainly to the improved functional integrity of micro-heterointerfaces owing to GSCs minimization.

We then obtained the PSC durability results under different external stressors following international standard protocols, as shown in **Figure 4d-f**.[4] We consider that Spiro-OMeTAD hole-transporting layers (HTLs) can have uncertain influence to the device durability results although using it is suitable for demonstrating the efficiency potential. Therefore, the PSC devices for these durability tests adopt PTAA HTLs. First, we monitored the PCE variations of PSCs under thermal fatigue stressors. The thermal-cycling test was performed in a program-controlled environmental chamber, following the ISOS-T-3 protocol that entails thermal cycles from -40°C to 85°C. For the PSC without GSCs, typically, 83% of the initial PCE is retained after 300 temperature cycles (**Figure 4d**), largely outperforming that (40%) of the regular PSC. Note that the initial PCEs of devices with and without GSCs in the ISOS-T-3 tests are typically 19.9% and 21.0%, respectively. **Figure 4g** illustrates the periodic compressive-tensile strain (**Supplementary Fig. 26**) caused by the difference in thermal expansion coefficients on the perovskite heterointerface during the thermal cycling test. Unlike the case of non-concaved grains, GSCs locally break the structural integrity of micro-heterointerfaces and leave nanovoids contained at the grain-CTL micro-heterointerface, leading to only mechanically weak grain ridge-based connections as shown in the right panel. This weak connection can easily cause delamination under interfacial fatigue because of the abnormal increase of interfacial stress in micro-interfaces with GSCs (**Supplementary Fig. 26**). **Supplementary Fig. 30** confirms that severe grain degradation and interfacial delamination have occurred after 300 thermal cycles for the pristine case, whereas for the non-concaved case, the high-integrity of the grain-CTL micro-heterointerface is retained. Then, we expect that the existence of these GSCs-induced nanovoids can accommodate the moisture and hinder the heat transfer at the micro-interface in the damp-heat test, as illustrated in the inset of **Figure 4h**. We evaluated the device durability under damp-heat conditions (85°C, 85%RH) following the ISOS-D-3 protocol. Typically, PSCs without GSCs can maintain 90% of their initial efficiency after 660 h testing (**Figure 4e**), and the regular PSC shows only 45%. Note that the initial PCEs of devices with and without GSCs are typically 20.3% and 21.5% in the ISOS-D-3 tests, respectively. The elimination of nanovoids in buried heterointerface (as natural hosts for moisture molecules), together with the homogenous distribution of TFSAP on interfaces with hydrophobic fluorocarbon chains, contributes to the better humidity durability in target devices (**Supplementary Fig. 21**). The homogeneous lateral temperature distribution and facilitated grain-SnO_2 heat transfer also promote better high-temperature durability in target devices (**Figure 3f-h**). Furthermore, we performed maximum power point (MPP) tracking tests following the ISOS-L-11 protocol. Typically, upon MPP operation for 1290 h, the PSC without GSCs still maintains 90% of the initial PCE (**Figure 4f**), whereas the regular device stands for only 144 h before the initial PCE drops to 90%. Note that the initial PCEs of devices with and without GSCs are typically 20.5% and 21.4% in the ISOS-L-11 -tests, respectively. Since GSCs introduce more free micro-surfaces which are not physically passivated by the SnO_2 ETL, it is not surprising that GSCs can serve as facile sites where the loss of stoichiometry can occur at the illustration side (**Figure 4i** inset), as demonstrated by the better rigorous photothermal stability of perovskite films without

GSCs (**Figure 3d-e**). In addition, excess photogenerated carriers localized at GSCs could not be effectively extracted by SnO_2 ETL (**Figure 3b**), which can induce charge accumulation and accelerate the perovskite degradation via enhanced ion activities.[31] The combination of excellent thermal cycling, damp-heat, and MPP tracking stabilities are comparable to the best in the literature.[5,32-36]

Finally, confirming the positive effects of GSCs minimization requires excluding the possible contributions from surfactant's chemical passivation and GBGs flattening. In this regard, we observed that there is strong consistency between the varying trend of the GSC angles and device PCEs by optimizing the TFSAP addition amount. Also, we used sodium dodecyl benzene sulfonate (SDBS; a classic surfactant molecule with sulfonic acid group) and PTFS (shorter carbon fluorine chain than TFSAP), we observed limited effects of these two molecules in altering the GSC geometry when the same additive concentration is applied as TFSAP, as shown in **Supplementary Fig. 28**. While these two are expected to exhibit similar chemical passivation effects at the molecule scale like TFSAP,[37,38] under our specific experimental conditions, we did not observe any notable increase in the PL intensity and device PCEs (**Supplementary Fig. 31**). Therefore, we deduce that the contribution of TFSAP to the device improvement is primarily from the observed GSC geometry optimization rather than its possible chemical passivation effects. Furthermore, we fabricated perovskite films with GBGs flattened to a similar angle θ using a previous reported method.[17] The AFM images of perovskite bottom surface and statistical distribution of GBG angle θ are shown in **Supplementary Fig. 32**. The *J-V* performance and device stability demonstrate a lower level of improvement as compared to the approach used in this work, dictating the nontrivial role of GSCs minimization on the overall device improvements. Finally, while an effective GSC elimination is found to contribute to the enhancement in device performance, there could also be other potentially negative factors triggered by the additives. Taking the P123 case as an example, to induce the GSC elimination, a relatively high additive concentration is used, which creates insulating surface and thus lead to an only limited PCE increase (**Supplementary Fig. 33**).

Conclusions

In summary, we have revealed a previously overlooked microstructure, GSC, and elucidated its microstructural evolution process, along with its detrimental effects on the structural integrity, charge-extracting, chemical stability, and thermomechanical reliability of the buried perovskite grain-CTL heterointerfaces Through using the surfactant molecule TFSAP to minimize GSCs, we have successfully constructed a robust perovskite heterointerface in PSCs, consisting near-ideal micro-heterointerface segments. The resultant PSC not only delivers an improved PCE of 25.5 % but also retains its initial efficiencies of 83%, 90%, and 90% after undergoing 300 thermal cycles (ISOS-T-3 protocol), 660 h of damp-heat exposure (ISOS-D-3 protocol), and 1290 h of MPP operation (ISOS-L-1l protocol), respectively. This study highlights a crucial but neglected perovskite surface microstructure type, and its nontrivial effects on the performance and durability of PSCs. The insights into the microscopic structure-property-performance relationship gained from this work can add to our established understandings and contribute to the broad efforts developing highly efficient and stable PSCs and other optoelectronic devices.

Methods

Raw materials. Tin (IV) oxide (15 wt.% in H_2O colloidal dispersion) was purchased from Alfa Aesar (USA). PbI_2 (99.99%), (3-iodopropyl)trimethoxysilane ($Si(OCH_3)_3(CH_2)_3I$, 95%) and 4-Isopropyl-4'-methyldiphenyliodonium Tetrakis(pentafluorophenyl)borate (TPFB, >98%) were purchased from TCI (Japan). $HC(NH_2)_2I$ (FAI, >99.99%), methylammonium chloride (MACl, >99.99%), 4-methoxy-phenethylammonium-iodide (MeO-PEAI, >99.99%) and FK 209 Co(III) TFSI salt were purchased from Greatcell Solar (Australia). CsI (99.999%) and PTAA was purchased from Xi'an Yuri Solar (China). Spiro-OMeTAD (99.8%) was purchased from Borun Chemical (China). Tridecafluorohexane-1-sulfonic acid potassium salt (TFSAP, 95%) was purchased from Macklin (China). Potassium chloride (KCl, 99.0-100.5%), poly(methylmethacrylate) (PMMA), 4-tert-butylpyridine (t-bp, 96%), Bis(trifluoromethane) sulfonimide lithium salt (99.95%), $PbBr_2$ (≥99%), dimethyl sulfoxide (DMSO, 99.9%), dimethylformamide (DMF, 99.8%), chlorobenzene (CB, 99.8%), toluene (TB, 99.8%), acetonitrile (ACN, >99.9%), Diethyl ether (DE, 99%) and isopropyl alcohol (IPA, 99.5%) were acquired from Merck (USA). Dichloromethane was purchased from International Laboratory USA.

Device Fabrication. The pre-patterned ITO substrates were cleaned by sonication with deionized water, acetone, and isopropanol for 15 min each. All substrates were cleaned by ultraviolet (UV)/ozone treatment for 30 min after drying by N_2 gas flowing. The SnO_2 colloid precursor was diluted with deionized water (v/v 1:5), and was spin-coated onto ITO substrates at 3000 rpm for 30s with a subsequent annealing at 180 °C for 30 min. The as-prepared SnO_2 film was treated by UV/ozone for 10 min before subsequent deposition. KCl solution (3 mg/mL in DI water) was spin-coated on the SnO_2 layer at a speed of 4000 rpm for 20 s with a subsequent annealing at 100 °C for 10 min. The perovskite film fabrication processes of two components were listed below. TFSAP mother solution was prepared in mixed DMF-DMSO solvent and was added into perovskite precursor to promote a concentration of 0.6 mg/mL in target perovskite film. The HTL solution were prepared by mixing 1 mL Spiro-OMeTAD solution (91 mg/mL in chlorobenzene) with 36 μL 4-tertbutylpyridine, 21 μL Li-TFSI solution (520 mg/mL in acetonitrile) and 16 μL FK209 solution (375 mg/mL in acetonitrile). Then 50 μL of HTL solution was spin-coated onto the perovskite layer at 3000 rpm for 30 s. Spiro-OMeTAD layer was placed in in a drying oven (humidity less than 5%) for 2 days to promote the oxidation process of Spiro-OMeTAD. For the stability test, PTAA was used to replace Spiro-OMeTAD. Herein 50 μL of PTAA solution (30 mg/ml in CB with 3 mg/ml TPFB doping) was spin-coated onto the perovskite layer at 2000 rpm for 30s. Finally, 80 nm Au was deposited by thermal evaporation. For device encapsulation, we applied UV glues at the device edges, following by a typical curing process.

$FA_{0.9}Cs_{0.1}PbI_3$ perovskite layer: This FA-Cs composition was used for fundamental investigation. The perovskite precursor solution was prepared by dissolving 36 mg CsI, 154.7 mg FAI and 461 mg PbI_2 in 1 mL mixed DMF-DMSO solvent (v/v 7:3). The precursor solution was stirred at room temperature overnight and then filtered before using. A 50 μL precursor solution was dripped onto the SnO_2 ETL surface. The spin-coating process was carried out in three steps: 500 rpm for 5 s, 3000 rpm for 10 s, and finally 5000 rpm for 30 s. At the 10 s of the final step, 400 μL of toluene was dropped onto the substrate within 1s. The deposited film was immediately annealed on a 170°C hotplate for 6 min.

$(FA_{0.95}Cs_{0.05}PbI_3)_{0.975}(MAPbBr_3)_{0.025}$ perovskite layer: This composition was used for high-PCE device demonstration. The perovskite precursor solution was prepared by dissolving 228.8 mg FAI, 18.2 mg CsI, 33.7 mg MACl, 705.3 mg PbI_2 and 18.2 mg $MAPbBr_3$ single crystal in 1 mL mixed DMF-DMSO (v/v 8:1). $MAPbBr_3$ single crystal was synthesized by mixing MABr and $PbBr_2$ in a 1:1 molar ratio with a concentration of 0.2 M in DMF solvent and capturing the single crystal with dichloromethane antisolvent. Then 60 μL precursor solution was dripped onto the SnO_2 layer, followed by a two-stage spin-coating process (1000 rpm for 10 s and 4000 rpm for 30 s). 800 μL diethyl ether was dropped onto the spinning perovskite surface within 2 s at the 15s of the second step. The wet film was annealed on a 100 °C hotplate for 40 min. After the film had been cooled to room temperature, 50 μL MeO-PEAI (dissolved in IPA; 4 mg/ml) passivation layer was spin-coated onto the perovskite layer at 5000 rpm for 30 s, followed by annealing at 100 °C for 5 min to improve overall V_{OC} of all PSC devices.

Materials and device characterization. The AFM topographic images of the perovskite layers were acquired using the Multimode 8 (Bruker, USA) with a RTESP-300 tip in non-contact tapping mode. A scanning electron microscope (Gemini 1530, LEO, Zeiss, Germany) was used for characterizing the top-view surface and cross-sectional SEM images. XRD (D8 Advance, Bruker, USA) with Cu Kα radiation (λ = 1.5406 Å) was used to characterize the crystallographic structure of the perovskite layer. The steady-state PL and TRPL signals were directed into a spectrograph (Ando Kymera 328i) with the excitation of a 375 nm picosecond laser (LDH-D-C-375, PicoQuant, Germany). The PL signal was further collected by an electron multiplying charge-coupled device (EMCCD; Andor iXon Life 888, Oxford Instruments, UK) for the steady-state PL and a single-photon avalanche photodiode for the TRPL measurements. For the measurement of PL from the bottom side of the fabricated perovskite films, a quartz was used to replace the ITO glass substrate to minimize light scattering. PL mapping images were captured by a digital microscope camera (Nikon DS-Qi2) with a UV light source (250-450 nm) and a filter (long pass after 726 nm). UV-vis spectra were acquired by a commercial UV-visible spectrophotometer (Cary 300, Agilent, USA).

The *J-V* characterization for perovskite devices was measured by a source meter (2612, Keithley, USA) under an AM 1.5G spectrum (one-sun illumination; 100 mW cm^{-2})

generated by an AAA-class solar simulator (Sirius-SS, Zolix, China) in a glovebox filled with nitrogen. All devices were measured in a reverse scan (from 1.3 V to -0.02 V) with a step size of 0.02 V and a delay time of 10 ms. The active area defined by a shadow mask was 0.05 cm^2. The light intensity was calibrated by an Oriel® reference solar cell accredited by NIST to the ISO-17025 standard. External quantum efficiency spectra were recorded at a chopping frequency of 165 Hz in AC mode on a solar cell quantum efficiency measurement system (QE-R3011, Enlitech, China). For the MPP tracking test of PSC devices, devices were placed inside a test chamber in a nitrogen glovebox, with a continuous flow of N_2 gas to maintain the temperature of test chamber to 40-50 °C, following the ISOS-L-1l protocol. The devices operated under bias at their maximum power points, with data points collected at regular intervals. For the thermal cycling stability test (ISOS-T-3 protocol), encapsulated devices were placed in an environmental chamber controlled by the self-defined program. The temperature was set to be cycled between -40 °C and +85 °C, with each cycle lasting 54 min. The temperature variation curve of a cycle (54 min) during the thermal cycling test is shown in **Supplementary Fig. 34**. The humidity was controlled to below 20% RH. The PCE test of devices was in the nitrogen glovebox on room temperature. For the damp heat stability test (ISOS-D-3 protocol), encapsulated devices were placed in an environmental chamber with a temperature of 85 °C and a humidity of 85% RH. The PCE test of devices was also in the nitrogen glovebox on room temperature.

For the measurement process of the side angles of GBGs and GSCs, in the sample preparation, we applied an epoxy glue on the PMMA-protected perovskite layer and then covered the film with a glass slide. Then, we stored the samples in a dark, dry box (RH<15%) until the epoxy was completely cured and reached its maximum bonding strength. We deliberately labelled the corresponding locations (using a glass cutter to pre-mark a grid on the glass backside of the substrate to label the SnO_2 region) to ensure the probed surfaces of SnO_2 top and perovskite bottom are from the correlated region. Similarly, a relatively smaller grid within the former was also pre-marked on the backside of the cover glass to label the perovskite region. **Supplementary Fig. 35** indicated that the spatial differences of AFM morphology can be considered negligible in corresponding locations. Then, we applied a force to delaminate the perovskite layer from the SnO_2 ETL. This method can effectively separate the perovskite bottom surface from the SnO_2 surface without degrading the perovskite film (in regions of sufficient area). Then, we performed high-resolution AFM scans on both SnO_2 top surface and perovskite bottom surface to acquire 2D height profiles. AFM height images were analyzed using NanoScope Analysis software (V1.8). From these images, profiles of grain boundary grooves and intragrain height were extracted. For the standardized perovskite film delamination test, samples with the structure ITO/SnO_2/perovskite/PMMA were fabricated firstly. The SnO_2 and perovskite layers were prepared as the method of PSC devices. Then PMMA solution (10 mg/mL in CB) was spin-coated at 3000 rpm for 30 seconds onto the perovskite surface, and samples were placed in a nitrogen glovebox until the solvent completely evaporated. PMMA layer was used to prevent a reaction between the epoxy resin and the perovskite layer.

A blade array with 1 mm spacing was used to scribe the sample surface for fabricating a standard grid. A thin layer of epoxy film (2 μm) was applied to glue a glass substrate onto the film structure, which is kept in the dry air glovebox (< 15% RH) for complete epoxy curing. The delaminated area ratio was calculated by comparing the number of perovskite grids on the peeled glass substrate to the number of total grids covered by epoxy. Rating the scale of interfacial adhesion was based on ASTM D3359 standard. 0B represented that the removed area from substrate is greater than 65%, corresponding to the poorest interfacial strength. 1B, 2B, 3B, and 4B represented the 35-65%, 15-25%, 5-15% and less than 5% removed area, respectively. 5B represented that no residual area on the substrate after delamination, corresponding to the strongest interfacial strength. For each GB and grain micro-surface, we conducted two measurements at different positions on it for the accuracy of θ and ξ.

For the thermal transport measurement, the IPVP TA experiments were performed for samples with a structure of Glass/ITO/SnO_2/Perovskite/PMMA. In IPVP TA experiments, the mid-infrared (MIR) pump pulses were produced from a high-energy MIR optical parametric amplifier (OPA; Orpheus-One-HE, Light Conversion). The OPA was powered by a Pharos amplifier with 170 fs pulse duration, 1030 nm wavelength, and 2 kHz repetition rate and reduced into 1 kHz by an optical chopper. The broadband probe pulses at a 2 kHz repetition rate were produced by a supercontinuum laser (DISCO-2-UV, Leukos), which was electronically triggered and delayed from the fs pump laser with a digital delay generator (DG645, Stanford Research Systems). The transmitted probe light was captured by a high-speed USB spectrometer (AvaSpec-ULS2048CL-EVO, Avantes). Perovskite and PMMA layers were kept about 100 and 30 nm thick, respectively. Samples were vibrationally excited by MIR pulses centered at 3170 nm (resonant with the N-H and C-H stretching modes), the pump-induced lattice temperature increase results in the transmittance change, which was captured by a time-delayed, broadband visible probe. Here, dT/T denotes the differential change in transmittance and is defined as $dT/T = (T(t) - T(0))/T(0)$, where $T(t)$ is the transmittance at delay time t after the pump excitation and $T(0)$ is the transmittance prior to the pump excitation.

The GaussAmp function was used to fit the curves on column diagrams in **Figure 1j** and **Supplementary Fig. 32**. The normal distribution curve was used to fit the column diagrams in **Figure 4c**.

OWRK method. In the OWRK method, according to the balance of forces at the three-phase contact point where air, liquid, and solid meet, Young's equation is written as

$$\gamma_{sv} = \gamma_{sl} + \gamma_{lv} \cos\theta \tag{1}$$

where γ_{sv} is the surface free energy of the solid, γ_{sl} is the interfacial tension between the liquid and solid, γ_{lv} is the surface tension and θ is the contact angle. The adhesion work is defined as:

$$W_a = \gamma_{sv} + \gamma_{lv} - \gamma_{sl} = \gamma_{lv}\left(1 + \cos\theta\right) \tag{2}$$

The combining rule proposed by the OWRK model is indicated below:

$$W_a = 2\left(\sqrt{\gamma_{sv}^D \gamma_{lv}^D} + \sqrt{\gamma_{sv}^P \gamma_{lv}^P}\right) \tag{3}$$

where γ_{sv}^D and γ_{lv}^D are dispersive components, γ_{sv}^P and γ_{lv}^P and are polar components of solid and liquid surface energies, respectively. Combined with Young's equation, we get

$$\gamma_{lv}\left(1+\cos\theta\right) = 2\left(\sqrt{\gamma_{sv}^D \gamma_{lv}^D} + \sqrt{\gamma_{sv}^P \gamma_{lv}^P}\right) \tag{4}$$

There are two unknown parameters γ_{sv}^D and γ_{sv}^P if the dispersive components and polar components of the probing liquid are known. Based on that, H_2O and diiodomethane with known dispersive and polar parts of surface tensions are selected to compute the solid surface free energy, with their parameters listed in **Supplementary Table 2**.

Mullins GBG model. The Mullins GBG model was utilized to determine the GB energy γ_{gb}, which can be calculated by the equation:

$$\frac{\gamma_{gb}}{\gamma_s} = 2\sin\left(\tan^{-1}\left(\frac{md}{2w}\right)\right) \tag{1}$$

where m is typically a constant equal to 4.73, w is the GBG width, and d is the GBG depth. Surface energy γ_s has been determined by the OWRK method. The depth and width values were measured using NanoScope Analysis software (V1.8). A total of 40 times measurements for the groove width and depth and the mean value of them was utilized to determine the value of γ_{gb} in **Figure 3c**.

GSC microstructure evolution induced by BTS. We propose a quantitative physical model to deduce the GSC formation process by BTS and explore the role of TFSAP on flattening GSCs.[21] This model offers a simplification by representing perovskite crystallites as a perfectly regular array of hexagonal crystallites to simulate the grain coalescence process. The size of each hexagonal crystallite is $2a$, with a height of h. The out-of-plane separation between adjacent crystallites is denoted as $\varDelta$. Let γ_1 represent the surface energy of the crystallite, γ_2 represent the grain boundary energy, M represents the Young's modulus, and v represent the Poisson's ratio. The free energy per unit film area of each crystallite before coalescence E_1 can be expressed as

$$E_1 = E_0 + \frac{2h\gamma_1}{a} \tag{1}$$

where E_0 represents the free energy per unit area regarding the upper and lower surfaces, while the second term denotes the free energy per unit area of the side surfaces. When crystallites coalesce, each crystallite is applied a biaxial elastic strain to fill the gaps, resulting in an out-of-plane strain of $\varepsilon = \varDelta_{xy}/2a$. In this process, two side surfaces will be consumed to form a new grain boundary. The free energy per unit film area of each crystallite before coalescence E_2 can be expressed as

$$E_2 = E_0 + \frac{h\gamma_2}{a} + \frac{M}{1-\upsilon} h \left(\frac{\Delta_{xy}}{2a} \right)^2 \tag{2}$$

where the second term represents grain boundary free energy per unit area and the third term denotes the strain energy per unit area. $M/(1-v)$ represents the biaxial modulus of the crystallites. Here, we did not consider the anisotropy of crystallites and the constraints from the substrate. When $E_2 < E_1$, the grain coalescence process is spontaneous. When $E_2 = E_1$, the maximum out-of-plane deformation Δ_{max} can be calculated, and we can determine the maximum biaxial tensile stress σ_{max}:

$$\Delta_{\max} = \left[4a\left(2\gamma_s - \gamma_{gb}\right)\frac{1-\upsilon}{M} \right]^{1/2} \tag{3}$$

$$\sigma_{\max} = \frac{M}{1-\upsilon}\frac{\Delta_{\max}}{2a} = \left(\frac{M}{1-\upsilon}\frac{2\gamma_s - \gamma_{gb}}{a} \right)^{\frac{1}{2}} \tag{4}$$

where γ_s and γ_{gb} are the surface energy and GB energy per unit area, respectively. The biaxial tensile stress can be very high even for small grains. Considering the less Young’s Module during thermal-induced coalescence, and the existence of ion plastic flow at grain surfaces, we speculated that surface deformation occurs via biaxial ion plastic flow for relaxing this high stress, finally leaving concaves at the grain surface.

Note that the elaborated theory above is only applicable to the standard case of each grain containing only one GSC, which is suitable for analyzing the perovskite film with a standard thickness (~300 nm) as in our work. In practice, we experimentally observed that when the film thickness is beyond the standard thickness, it become evident that one grain can contain multiple GSCs, calling for the need of modifying the theory for further illustrating the GSCs formation.

Multiscale FEA simulation

The simulation of the micro-heterointerface was conducted using the finite element analysis. The thermomechanical parameters of materials were collected in **Supplementary Table 3**.

For the simulation of heat transfer at the micro-interface, only perovskite and adjacent SnO_2 layer were induced. The scale of the perovskite and SnO_2 layers were set at 500 × 300 nm^2 and 500 × 30 nm^2, respectively. GSCs were modeled by adding a crescent-shaped air gap with a length of 460 nm and a depth of 10 nm at the interface. In the case of internal thermal sources, the middle region of perovskite film needed to be a thermal source with a constant high temperature. Therefore, the height of the perovskite grain was reset to 150 nm, and the top boundary (corresponding to the middle region) was set to be a high temperature. In the models with and without GSC, we divided the geometry into 3464 and 2324 triangular elements, respectively. In the solid heat transfer simulation, interfacial thermal resistance was not considered. Boundaries without an initial temperature set was considered thermally insulated.

For the thermal stress and solid elastic deformation simulation, Au (80 nm), Spiro-OMeTAD (30 nm), perovskite (300 nm), SnO_2 (30 nm), and ITO (140 nm) layers were all constructed to take the device integrity into consideration. GSCs were modeled as the same as the heat transfer simulation. In the models with and without GSC, we divided the geometry into 2564 and 1704 triangular elements, respectively. For simplifying the computing, we did not construct the glass substrate with a thickness of 1.1 mm. But we set the bottom boundary of ITO layer as the rigid boundary, considering the restriction of the thick glass substrate. After setting the boundary conditions for temperature, the temperature distribution was first calculated. The temperature values were then used as initial values for subsequent simulations of thermal stress and elastic deformation.

Data Availability

All data that support the main findings are available in the main text, the Supplementary Information and Data Source files.

Acknowledgments

Y.Z. acknowledges the Excellent Young Scientists Funds (No. 52222318) from the National Natural Science Foundation of China (NSFC), the Early Career Scheme (No. 22300221), General Research Fund (No. 12302822), & NSFC/RGC Collaborative Research Scheme (No. CRS_HKUST203/23) from the Hong Kong Research Grant Council (RGC). X.T. acknowledge the support of Hong Kong PhD Fellowship and the administrative support of Prof. S.-K. So at HKBU. The research at Yale University was primarily supported by the U.S. National Science Foundation (No. DMR-2313648).

Author contributions

Y. Zhou conceived the idea and supervised the project. Y. Zhou performed the technology innovation. Y. Zhou and T.X. co-designed the experiments. T.X. fabricated and tested the solar cell devices, characterized material samples (AFM, UV-vis, PL mapping, delamination tests, etc.), and carried out the multiscale FEA simulation. M.H. and Y. Zhang assisted the SEM and AFM characterizations. T.D. performed the XRD characterization. Y.L. and P.G. performed the spectroscopic measurements for PL and thermal transport measurements. T.X. and Y. Zhou drafted the manuscript. All co-authors have contributed to reviewing and revising the manuscript.

Competing interests

A United States Provisional Utility Patent was filed based on the technology innovation of this work. The authors declare no other competing interests.

Figure 1. Geometric characteristics and chemical tailoring of GSC microstructures at the perovskite grain-CTL micro-heterointerface. a, b, AFM topography of the perovskite film bottom surfaces with and without GSCs at the grain-CTL heterointerfaces, respectively. **c-f,** 2D AFM images (**c, d**) and 3D AFM images (**e, f**) of the selected regions (red-dashed lines) in perovskite film bottom surfaces with and without GSCs, respectively. The grain (**c, e**) contains a micro-surface with concaved centers surrounded by adjacent convex ridges and GBGs, while the grain (**d, f**) contains a nearly flat micro-surface. **g, h,** 2D surface height line-profile (guided by blue dashed lines) on perovskite film bottom surfaces with (**c**) and without GSCs (**d**), respectively. The typical surface height line-profile (guided by blue dashed lines in **Supplementary Fig. 2a**) of the SnO_2 ETL top surface is also shown to demonstrate the difference in the heterointerfacial integrity. As seen, GSCs on pristine grains create obvious nanovoids in micro-interfaces while target grains do not. **i,** Schematic illustration showing the topography of the surface of flipped perovskite grains at the heterointerface. The angles illustrated using blue and red lines correspond to GBG angle θ and GSC angle ξ, respectively. θ is defined as the angle between the tangent to the GBG side and the horizontal direction, while ξ is defined as the angle between the line connecting the apex of the convex ridge to the center of the GSC and the horizontal direction. **j**, Statistical distributions of GBG angle θ of perovskite films with GSCs (sample size n = 40) and without GSCs (sample size n = 40). **k**, Statistical distributions of GSC angle ξ of perovskite films with GSCs (sample size n = 30) and without GSCs (sample size n = 30). The box plot displays the mean, median line, upper minima and lower maxima, 25~75% box limits with 1.5× interquartile range whiskers.

Figure 2. Microstructural evolution of GSCs at the perovskite grain-CTL micro-interface. a, Schematic illustration of microstructural evolution of GSCs. Upon the grain growth of perovskites, the side surfaces of perovskite grains will gradually approach each other. In grain coalescence, it eventually causes the bonding of adjacent grain surfaces, as illustrated using the horizontal black dashed lines between perovskite structures within grains, forming GBs. The bonding-induced biaxial interatomic force F initially induces lateral deformation ε_{xy}, thus causing an out-of-plane deformation ε_z (labeled using blue boxes) owing to the global Poisson effect (left panel). In grain coarsening, GB grooving is lasting, in which solid-state ion continuously diffuses from the groove to convex ridges aside (middle panel). Finally, GSC (labeled using a semi-transparent blue box) forms under these two mechanistic processes, along with the generation of convex ridges (labelled using yellow semi-transparent boxes) (right panel). **b**, Schematic illustration of the role of TFSAP in tailoring GSCs. TFSAP, containing a short carbon-fluorine chain, a sulfonic acid and potassium ion (left panel), is expected to homogenously interact with perovskite surface/interface. It lowers the ε_{z_BTS} via manipulating surface energies and GB energies (middle panel) and suppresses the ion diffusion in GB grooving (right panel), thereby minimizing the formation of GSCs. **c,** The determined surface free energy γ_s, GB energy γ_{gb} and the $\Delta\gamma$ in the perovskite grains with and without GSCs. **d**, The normalized out-of-plane deformation ε_{z_BTS} in the perovskite grains with and without GSCs.

Figure 3. The optoelectronic, chemical, heat-transfer and thermomechanical properties of the perovskite grains-CTL micro-interface. **a,** Steady PL spectra of perovskite films with and without GSCs. **b,** Normalized TRPL spectra with biexponential fitting lines of perovskite films with and without GSCs. **c,** The current-voltage (*I-V*) curves with exponential fitting lines for the ohmic and trap-filled limited regions for the capacitor-like perovskite devices with the structure of ITO/SnO_2/perovskite/PCBM/Ag. **d-e,** Ultra-violet visible (UV-vis) absorption variations of perovskite films with and without GSCs under rigorous photothermal tests for 120 h (3-sun-intensity illumination; 80 °C), respectively. The inset is the optical photograph of degraded perovskite films after the test. **f-g,** The normalized transparent differential change in transmittance (*dT/T*) spectra at different pump delay times from 30 ns to 90 ns of perovskite samples with and without GSCs, respectively. **h**, The temperature distribution by FEA of the grain-CTL micro-interface with (top) and without GSCs (bottom). In this case of the internal thermal source, the temperature gradient is set from the top surface of the grain (85°C) to the bottom surface of SnO_2 layer (20°C). **i,** Schematic illustration of the delamination process for quantitively determining the mechanical reliability of the perovskite-CTL heterointerface. Standard perovskite grids are prefabricated on perovskite films by blade arrays and followed by a delamination process. The proportion of the delaminated area on the epoxy reflects the toughness level of the heterointerface. **j, k,** Optical photographs showing perovskite film residual areas on the CTL surface after the delamination process for the cases with and without GSCs, respectively. **l,** Statistical distributions of the normalized delaminated area A_d of perovskite films with GSCs (pristine, sample size $n = 21$; with I-SAM, sample size $n = 7$) and without GSCs (pristine, sample size $n = 22$; with I-SAM, sample size $n = 9$) after the delamination process. The box plot displays the mean, median line, upper minima and lower maxima, 25~75% box limits with 1.5× interquartile range whiskers. **m,** Statistical distribution of the scale (0B-5B) for rating the interfacial adhesion based on the normalized delamination area according to the ASTM D3359 standard. 0B represents that the removed area from substrate is greater than 65%, corresponding to the poorest interfacial strength. 1B, 2B, 3B, and 4B represent the 35-65%, 15-25%, 5-15% and less than 5% removed area, respectively. 5B represents no residual area on the substrate after delamination, corresponding to the strongest interfacial strength.

Figure 4. PCE and durability of PSC devices with and without GSCs at the perovskite grains-CTL micro-interface. a-b, *J–V* curves (**a**) and EQE spectra with integrated J_{SC} (**b**) of the champion PSCs with and without GSCs (reverse scan). The device structure is ITO/SnO_2/$(FA_{0.95}Cs_{0.05}PbI_3)_{0.975}(MAPbBr_3)_{0.025}$ perovskite/Spiro-OMeTAD/Au. The inset table in (**a**) shows the extracted *J-V* parameters. **c**, PCEs statistical distributions based on a total of 30 PSCs devices with and without GSCs. **d,** Thermal cycling durability (between -40 and +85 °C) of PSCs with and without GSCs based on ISOS-T-3 protocol. **e,** Damp heat durability of PSCs with and without GSCs based on ISOS-D-3 protocol (85°C; 85%RH). **f,** MPP tracking of PSCs with/without

GSCs based on ISOS-L-1I protocol (one-sun-intensity illumination; in N_2). N_2 gas flow was used for heat dissipation on the device surface, maintaining the temperature at around 40-50°C. The device structure for **d-f** is ITO/SnO_2/$FA_{0.9}Cs_{0.1}PbI_3$ perovskite/PTAA/Au. **g,** Schematic illustration of the strain evolution in perovskite film during -40°C to 85°C thermal cycling (left panel), which easily causes the interfacial delamination at the grain-CTL micro-heterointerface in the presence of the GSC because of the accumulated thermal stress on convex ridges, as shown in the right panel. **h**, Schematic illustration of the role of GSCs at micro-heterointerface in damp-heat test. GSCs can effectively facilitate the moisture ingression and hinder the grain-CTL heat transfer, resulting in moisture and heat accumulation at the micro-heterointerface. **i,** Schematic illustration of the photothermal decomposition that can easily occur at the exposed free surface of GSCs.

References

1 NREL Best Research-Cell Efficiency Chart, https://www.nrel.gov/pv/cell-efficiency.html

2 Park, J. *et al.* Controlled growth of perovskite layers with volatile alkylammonium chlorides. *Nature* **616**, 724-730 (2023).

3 Yu, S. *et al.* Homogenized NiO_x nanoparticles for improved hole transport in inverted perovskite solar cells. *Science* **382**, 1399-1404 (2023).

4 Khenkin, M. V. *et al.* Consensus statement for stability assessment and reporting for perovskite photovoltaics based on ISOS procedures. *Nat. Energy* **5**, 35-49 (2020).

5 Jiang, Q. *et al.* Towards linking lab and field lifetimes of perovskite solar cells. *Nature* **623**, 313-318 (2023).

6 Suo, J. *et al.* Multifunctional sulfonium-based treatment for perovskite solar cells with less than 1% efficiency loss over 4,500-h operational stability tests. *Nat. Energy* (2024).

7 Zhou, Y., Herz, L. M., Jen, A. K. Y. & Saliba, M. Advances and challenges in understanding the microscopic structure–property–performance relationship in perovskite solar cells. *Nat. Energy* **7**, 794-807 (2022).

8 Macpherson, S. *et al.* Local nanoscale phase impurities are degradation sites in halide perovskites. *Nature* **607**, 294-300 (2022).

9 Duan, T., Wang, W., Cai, S. & Zhou, Y. On-Chip Light-Incorporated In Situ Transmission Electron Microscopy of Metal Halide Perovskite Materials. *ACS Energy Lett.* **8**, 3048-3053 (2023).

10 Schulz, P., Cahen, D. & Kahn, A. Halide Perovskites: Is It All about the Interfaces? *Chem. Rev.* **119**, 3349-3417 (2019).

11 Ma, C. *et al.* Unveiling facet-dependent degradation and facet engineering for stable perovskite solar cells. *Science* **379**, 173-178 (2023).

12 Chen, P. *et al.* Multifunctional ytterbium oxide buffer for perovskite solar cells. *Nature* **625**, 516-522 (2024).

13 Dai, Z. *et al.* Interfacial toughening with self-assembled monolayers enhances perovskite solar cell reliability. *Science* **372**, 618-622 (2021).

14 T. Duan, S. You, M. Chen, W. Yu, Y. Li, P. Guo, J.J. Berry, J.M. Luther, K. Zhu, Y. Zhou. *Science* (2024) DOI:10.1126/science.ado5172.

15 Wang, M., Fei, C., Uddin, M. A. & Huang, J. Influence of voids on the thermal and light stability of perovskite solar cells. *Sci. Adv.* **8**, eabo5977 (2022).

16 Hu, H. *et al.* Void-free buried interface for scalable processing of p-i-n-based $FAPbI_3$ perovskite solar modules. *Joule* **7**, 1574-1592 (2023).

17 Hao, M. *et al.* Flattening Grain-Boundary Grooves for Perovskite Solar Cells with High Optomechanical Reliability. *Adv. Mater.* **35**, 2211155 (2023).

18 Luo, C. *et al.* Engineering the buried interface in perovskite solar cells via lattice-matched electron transport layer. *Nat. Photon.* **17**, 856-814 (2023).

19 Fei, C. *et al.* Lead-chelating hole-transport layers for efficient and stable perovskite minimodules. *Science* **380**, 823-829 (2023).

20 Chen, S. *et al.* Stabilizing perovskite-substrate interfaces for high-performance perovskite modules. *Science* **373**, 902-907 (2021).

21 Nix, W. D. & Clemens, B. M. Crystallite coalescence: A mechanism for intrinsic tensile stresses in thin films. *J. Mater. Res.* **14**, 3467-3473 (1999).

22 Wang, X. *et al.* Long-chain anionic surfactants enabling stable perovskite/silicon tandems with greatly suppressed stress corrosion. *Nat. Commun.* **14**, 2166 (2023).

23 Wang, L. *et al.* Surfactant engineering for perovskite solar cells and submodules. *Matter* **6**, 2987-3005 (2023).

24 Xue, J. *et al.* Crystalline Liquid-like Behavior: Surface-Induced Secondary Grain Growth of Photovoltaic Perovskite Thin Film. *J. Am. Chem. Soc.* **141**, 13948-13953 (2019).

25 Syed, K., Motley, N. B. & Bowman, W. J. Heterointerface and grain boundary energies, and their influence on microstructure in multiphase ceramics. *Acta Mater.* **227**, 117685 (2022).

26 Peng, W. *et al.* Reducing nonradiative recombination in perovskite solar cells with a porous insulator contact. *Science* **379**, 683-690 (2023).

27 Yang, Y. *et al.* Inverted perovskite solar cells with over 2,000 h operational stability at 85 °C using fixed charge passivation. *Nat. Energy* **9**, 37-46 (2024).

28 Zhang, S. *et al.* Minimizing buried interfacial defects for efficient inverted perovskite solar cells. *Science* **380**, 404-409 (2023).

29 Li, S., Dai, Z., Li, L., Padture, N. P. & Guo, P. Time-resolved vibrational-pump visible-probe spectroscopy for thermal conductivity measurement of metal-halide perovskites. *Rev. Sci. Instrum.* **93**, 053003 (2022).

30 Dai, Z. & Padture, N. P. Challenges and opportunities for the mechanical reliability of metal halide perovskites and photovoltaics. *Nat. Energy* **8**, 1319-1327 (2023).

31 Lin, Y. *et al.* Excess charge-carrier induced instability of hybrid perovskites. *Nat. Commun.* **9**, 4981 (2018).

32 Wang, H. *et al.* Interfacial Residual Stress Relaxation in Perovskite Solar Cells with Improved Stability. *Adv. Mater.* **31**, 1904408 (2019).

33 Li, G. *et al.* Highly efficient p-i-n perovskite solar cells that endure temperature variations. *Science* **379**, 399-403 (2023).

34 Yang, N. *et al.* Improving Heat Transfer Enables Durable Perovskite Solar Cells. *Adv. Energy Mater.***12**, 2200869 (2022).

35 Wang, T. *et al.* Room temperature nondestructive encapsulation via self-crosslinked fluorosilicone polymer enables damp heat-stable sustainable perovskite solar cells. *Nat. Commun.***14**, 1342 (2023).

36 Yuan, G. *et al.* Inhibited Crack Development by Compressive Strain in Perovskite Solar Cells with Improved Mechanical Stability. *Adv. Mater.* **35**, 2211257 (2023).

37 Wang, T. *et al.* High efficiency perovskite solar cells with tailorable surface wettability by surfactant. *J. Power Sources* **448**, 227584 (2020).

38 Zou, Y. *et al.* Sodium Dodecylbenzene Sulfonate Interface Modification of

Methylammonium Lead Iodide for Surface Passivation of Perovskite Solar Cells. *ACS Appl. Mater. Inter.* **12**, 52643-52651 (2020).

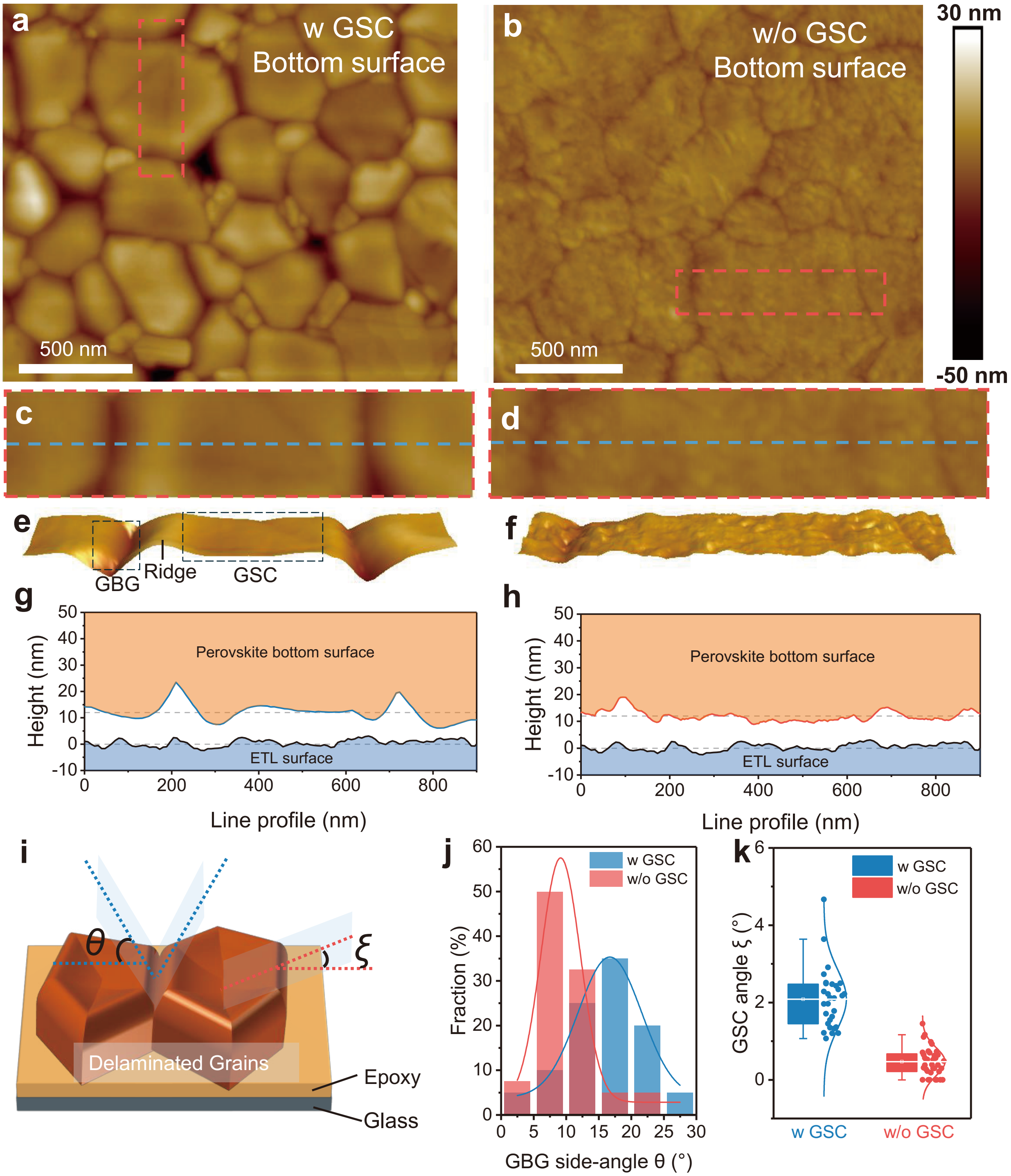
a
w GSC
Bottom surface
500 nm
b
w/o GSC
Bottom surface
500 nm
30 nm
-50 nm
c
d
e
GBG
Ridge
GSC
f
g
Height (nm)
Perovskite bottom surface
ETL surface
Line profile (nm)
h
Height (nm)
Perovskite bottom surface
ETL surface
Line profile (nm)
i
θ
ξ
Delaminated Grains
Epoxy
Glass
j
w GSC
w/o GSC
Fraction (%)
GBG side-angle θ (°)
k
w GSC
w/o GSC
GSC angle ξ (°)
w GSC
w/o GSC

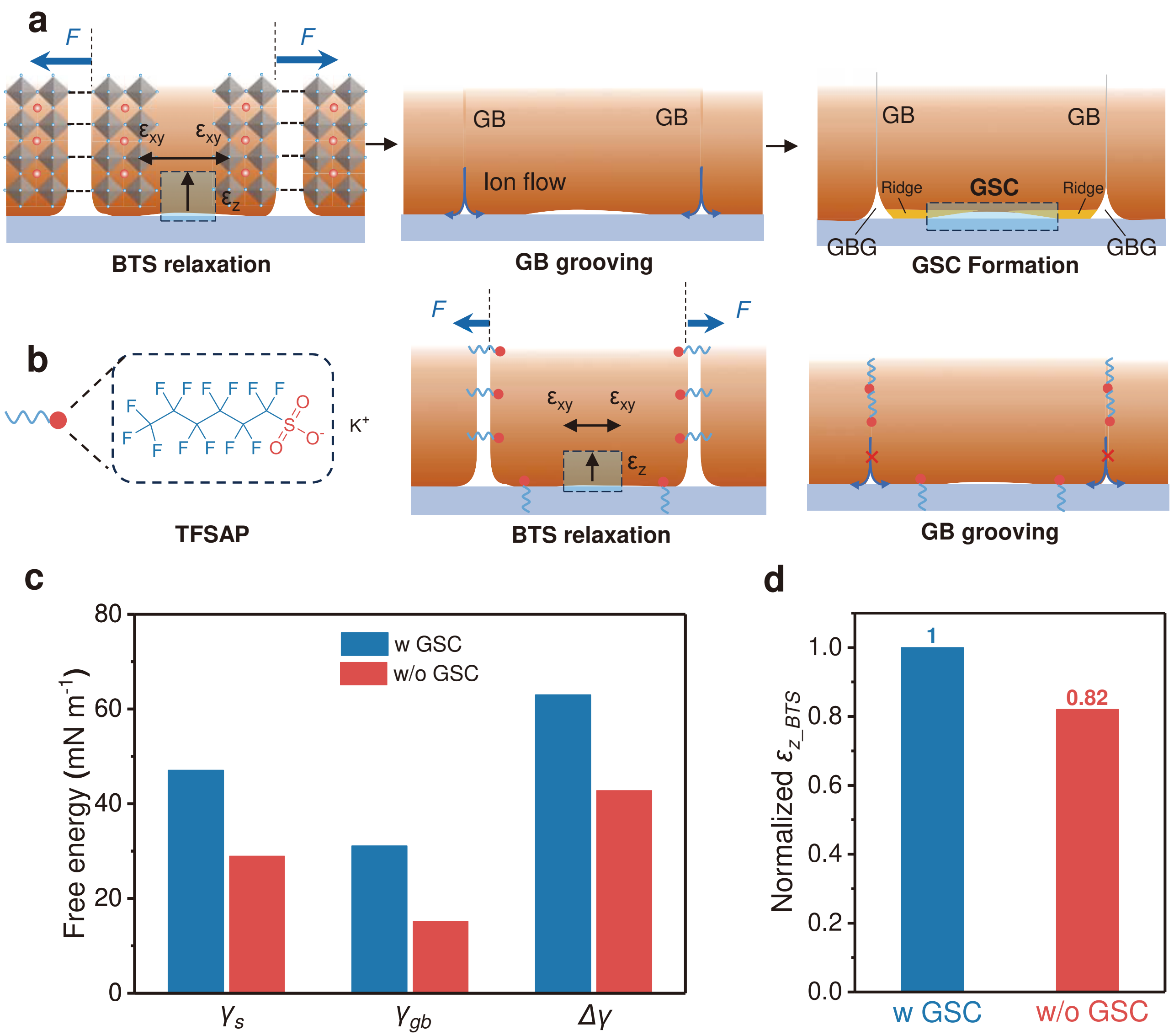
a
F
F
ε_{xy}
ε_{xy}
ε_z
BTS relaxation
GB
GB
Ion flow
GB grooving
GB
GB
Ridge
GSC
Ridge
GBG
GBG
GSC Formation
b
F
F
F
F
F
F
F
F
F
F
F
F
F
S
O
O
O-
K+
TFSAP
ε_{xy}
ε_{xy}
ε_z
BTS relaxation
GB grooving
c
Free energy (mN m-1)
80
60
40
20
0
w GSC
w/o GSC
γ_s
γ_{gb}
$\Delta\gamma$
d
Normalized ε_{z_BTS}
1.0
0.8
0.6
0.4
0.2
0.0
1
0.82
w GSC
w/o GSC

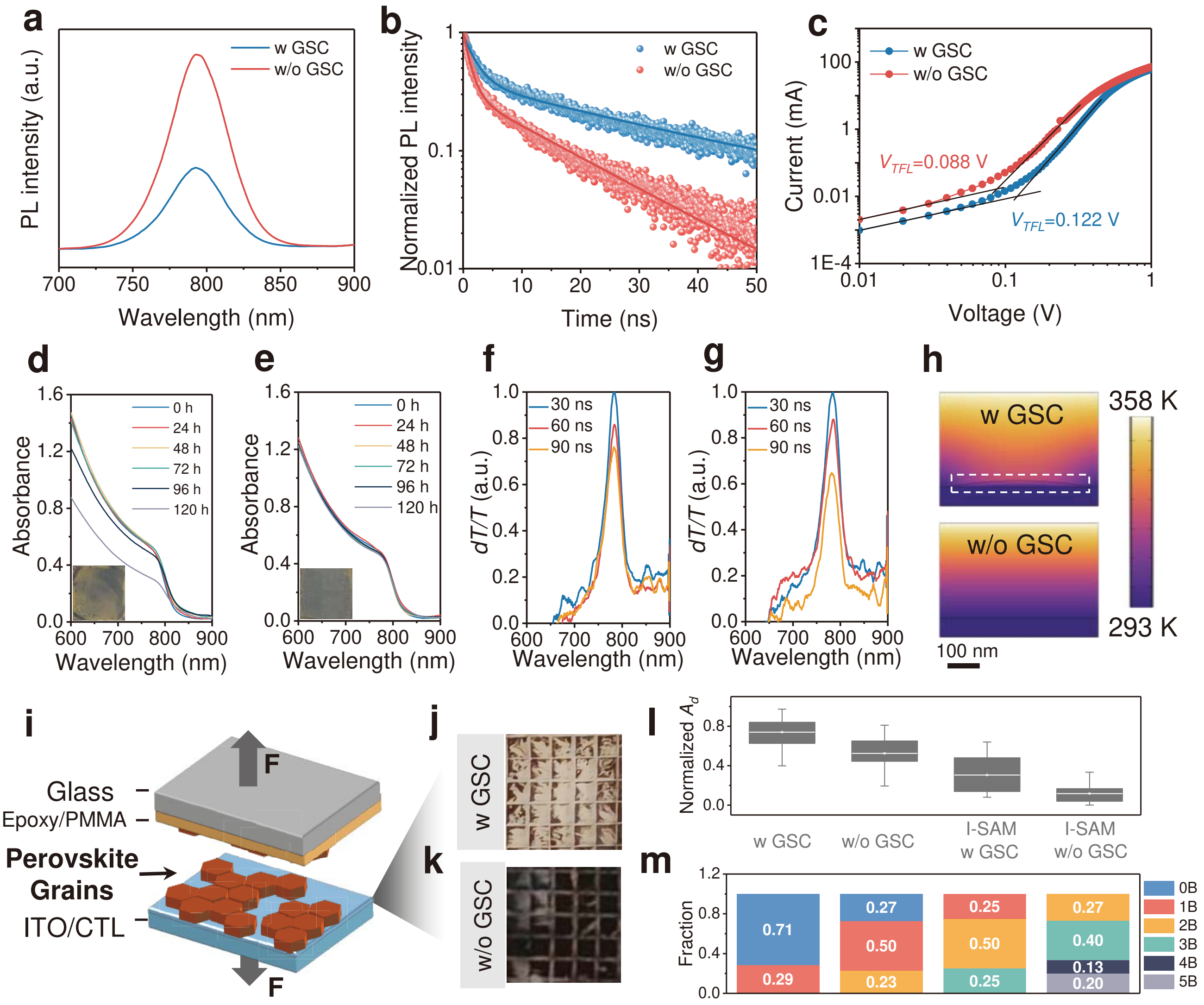
a
PL intensity (a.u.)
w GSC
w/o GSC
700 750 800 850 900
Wavelength (nm)
b
Normalized PL intensity
1
0.1
0.01
0 10 20 30 40 50
Time (ns)
w GSC
w/o GSC
c
Current (mA)
100
1
0.01
1E-4
0.01 0.1 1
Voltage (V)
w GSC
w/o GSC
V_{TFL}=0.088 V
V_{TFL}=0.122 V
d
Absorbance
1.6 1.2 0.8 0.4 0.0
600 700 800 900
Wavelength (nm)
0 h
24 h
48 h
72 h
96 h
120 h
e
Absorbance
1.6 1.2 0.8 0.4 0.0
600 700 800 900
Wavelength (nm)
0 h
24 h
48 h
72 h
96 h
120 h
f
dT/T (a.u.)
1.0 0.8 0.6 0.4 0.2 0.0
600 700 800 900
Wavelength (nm)
30 ns
60 ns
90 ns
g
dT/T (a.u.)
1.0 0.8 0.6 0.4 0.2 0.0
600 700 800 900
Wavelength (nm)
30 ns
60 ns
90 ns
h
w GSC
w/o GSC
358 K
293 K
100 nm
i
F
Glass
Epoxy/PMMA
Perovskite Grains
ITO/CTL
F
j
w GSC
k
w/o GSC
l
Normalized A_d
0.8
0.4
0.0
w GSC
w/o GSC
I-SAM w GSC
I-SAM w/o GSC
m
Fraction
1.2 0.8 0.4 0.0
0.71
0.29
0.27
0.50
0.23
0.25
0.50
0.25
0.27
0.40
0.13
0.20
0B
1B
2B
3B
4B
5B

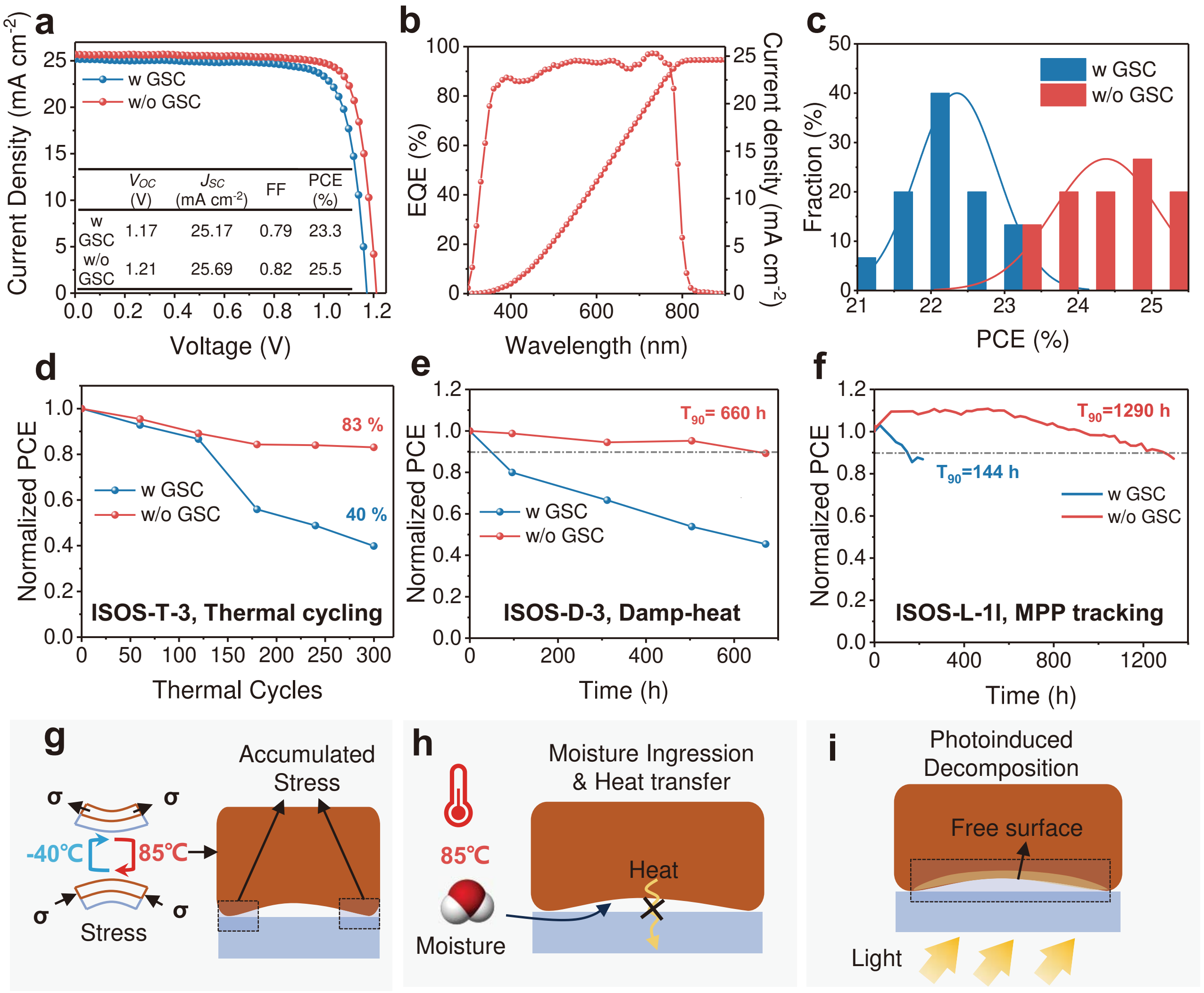

	V_{OC} (V)	J_{SC} (mA cm^{-2})	FF	PCE (%)
w GSC	1.17	25.17	0.79	23.3
w/o GSC	1.21	25.69	0.82	25.5